Mechanistic Analysis of the Oxygen Reduction Reaction at (La,Sr)MnO_3 Cathodes in Solid Oxide Fuel Cells

Anne C. Co and Viola I. Birss*

Department of Chemistry, The University of Calgary, 2500 University Drive NW, Calgary, Alberta, Canada T2N 1N4

Received: January 5, 2006; In Final Form: March 31, 2006

The primary aim of this work was to establish the mechanism of the oxygen reduction reaction (ORR) at $(La_{0.8}Sr_{0.2})_{0.98}MnO_3$ (LSM)-based cathodes in solid oxide fuel cells. Rate equations, based on the Butler−Volmer equation and employing either Langmuir or Temkin adsorption conditions for reactant and intermediate species, were derived, yielding predicted reaction orders and transfer coefficients. Experimental data were collected using half-cell cyclic voltammetry in a variable pO_2 atmosphere (0.03 to 1 atm) at 600 to 900 °C, using both dense and porous LSM-based cathodes, employed to establish the impact of the accessibility of the active site on cathode activity. The rate of the ORR at dense LSM has been found to be limited by the dissociation of O^-_{2ads} at low currents and by the first electron-transfer step, reducing O_{2ads} to O^-_{2ads}, at high currents. However, at porous LSM cathodes, the reaction mechanism is more difficult to deduce because the electrode morphology impacts significantly on the measured kinetic and mechanistic parameters, giving anomalous transfer coefficients of <0.5.

1. Introduction

The desire for a pollution-free environment, as well as our diminishing energy resources, has spawned the movement toward cleaner and more efficient sources of energy. One technology that minimizes the use of nonrenewable fossil fuels and produces no particulates or NOx is the fuel cell, a highly efficient means of converting chemical to electrical energy and heat.[1] Fuel cells are electrochemical devices, very similar to batteries, which produce electricity by reacting fuels, such as hydrogen or hydrocarbons, at the anode, and oxygen at the cathode, separated by an electrolyte. However, unlike batteries, a fuel cell does not need to be recharged and will continue to produce electricity as long as the fuel and oxidant are supplied to the electrodes.

In the case of solid oxide fuel cells (SOFCs), the electrolyte is an O^{2-} conducting ceramic, normally yttrium stabilized zirconia (YSZ), which has a conductivity comparable to aqueous solutions when heated to >700 °C. The cathode, where O_2 is reduced to O^{2-}, is normally $LaSrMnO_3$ (LSM), but recent work[2,3] has been focused on cathodes such as $LaCoO_3$, doped with lower valence metal ions. The fuel is typically oxidized at a Ni−YSZ composite anode, with the products combining with O^{2-} to form H_2O (and CO_2, when carbonaceous fuels are employed). The main advantage of SOFCs over the more widely studied low-temperature proton exchange membrane fuel cells (PEMFCs) is their fuel flexibility, related to their higher operating temperatures (>700 °C). Under these conditions, fuels such as CH_4,[4−6] alcohols,[7] CO,[8] and so forth, can be oxidized or reformed directly at the anode, without surface poisoning, thus allowing the use of the existing hydrocarbon infrastructure, while also achieving very high energy conversion efficiencies. Moreover, SOFCs generate high-grade heat during operation, where the rejected heat from the fuel cell can be used for the cogeneration of power.

This work focuses on the oxygen reduction reaction (ORR), which is known to limit the overall SOFC performance. The literature[9] generally describes the ORR mechanism as involving either a surface or bulk pathway. In the former, O_2 reacts only at the triple phase boundary (tpb), where the reactive gas meets the electrode and the electrolyte phases. Adsorbed O_2 is then reduced to either O^- or O^{2-}, followed by the transfer of O^{2-} through the electrolyte to the Ni anode. In the bulk pathway model, O_2 can react anywhere on the cathode surface, forming oxide anions which then diffuse into the bulk of the electrode material and then to the electrolyte. The surface pathway will occur at cathode materials that are electronically conducting, but not O^{2-} conductors, such as Pt or $LaMnO_3$ doped with ions such as Sr^{2+}, while the bulk pathway is anticipated for mixed ionic and electronic conductors, such as Sr-doped $LaCoO_3$ or $(LaSr)(CoFe)O_3$. Since LSM is a very good electronic conductor, but has negligible ionic conductivity, the ORR likely occurs via the surface pathway at the tpb.

The fundamental relationship which normally governs electron-transfer processes is the Butler−Volmer (eq 1), which shows the dependence of the net current density, i, on the overpotential (η)

$$i = i_o[e^{\alpha_a F\eta/RT} - e^{\alpha_c F\eta/RT}] \quad (1)$$

where[10,11] i_o is the exchange current density (the inherent reaction rate); α_a and α_c are the anodic and cathodic transfer coefficients, respectively, and contain a number of parameters including: the symmetry factor (β), the total number of electrons employed per O_2 molecule (n), the number of occurrences of the rate-limiting step (ν), and the number of electrons passed in the limiting step; F, R, and T have their usual meaning.

At high cathodic overpotentials (high-field conditions), the anodic reaction can be ignored and thus the second term in eq

* To whom correspondence should be addressed. Tel: (403) 220 6432. Fax: (403) 289 9488. E-mail: birss@ucalgary.ca.

10.1021/jp060099h CCC: $33.50
Published on Web 05/24/2006

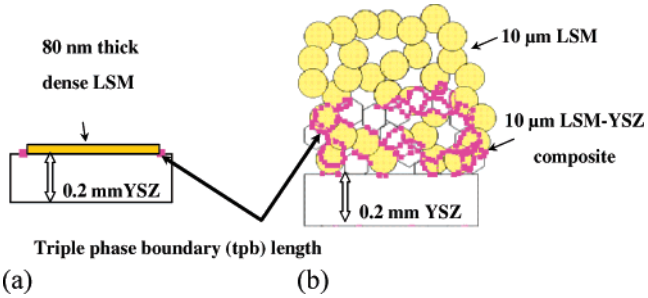

Figure 1. Schematic showing the location of reaction sites (tpb) in (a) a dense LSM cathode layer on a YSZ disk and in (b) a porous LSM-YSZ composite layer deposited on a YSZ disk.

1 dominates the measured current, giving eq 2. Rearrangement then gives the rate of increase of overpotential per decade of current density, that is, the Tafel slope (eq 3).

$$\log i = \log|i_o| + \frac{-\alpha_c F\eta}{2.303RT} \tag{2}$$

$$\text{Tafel slope} = \text{TS} = \frac{2.303RT}{\alpha_c F} \tag{3}$$

Equation 3 shows that the Tafel slope depends linearly on temperature, and for ease of comparison of ORR data collected at 600 to 800 °C, α is reported in the present work. Using normal mechanistic considerations, and assuming that $\beta = 0.5$,[10,11] α will take on values of 0.5, 1, 1.5, and so forth, depending on the position of the rate-limiting step in a series of reaction steps. Tafel slopes ranging between 250 and 450 mV (α values of 0.8 and 0.5, respectively) have been reported in the SOFC literature for the ORR at dense and porous LSM-based cathodes at 700 to 950 °C.[12] However, a detailed mechanistic analysis of the ORR, based on Tafel slopes, has not been a commonly used approach to date in SOFC studies.

The Butler−Volmer relationship can also be rearranged, as suggested by Allen and Hickling (AH),[13] giving eq 4, allowing the α values to be determined over the full range of η from a plot such as that shown in Figure 2b in the present work (using the data from Figure 2a). This allows the determination of the rate-determining step (rds), even at very low overpotentials.

$$\ln\left[\frac{i}{e^{nF\eta/\upsilon RT} - 1}\right] = \ln i_o - \frac{\alpha_c F\eta}{RT} \tag{4}$$

This paper focuses on using experimentally collected i/η data to identify the rate-limiting step of the ORR at LSM-based cathodes at >600 °C, with the primary goal being to knowledgeably improve the performance of LSM-based SOFCs. Our approach commences with the derivation of rate equations, assuming Butler−Volmer formulations, thus predicting α values and the reaction order with respect to O_2 for four possible ORR mechanisms. As the literature strongly suggests that the adsorption of reactants and intermediates plays a major role in the ORR under SOFC conditions,[14] we assume here that these processes obey either Langmuir or Temkin adsorption conditions, the most commonly encountered adsorption isotherms.

Two different LSM cathode geometries have been employed in this work (Figure 1). In the first case, a dense, disc-shaped LSM cathode was deposited on a fully densified YSZ electrolyte (Figure 1a), such that the ORR active sites (the tpb) are located only along the measurable perimeter of the LSM disk and are fully accessible to O_2. In the second case (Figure 1b), a porous, LSM-YSZ composite layer was employed, with the active tpb

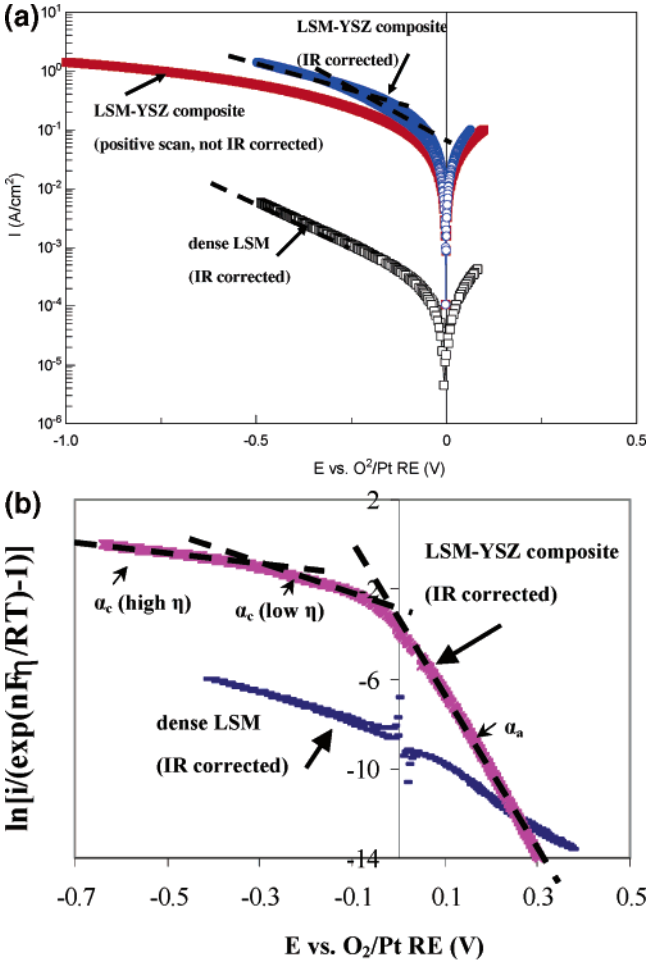

Figure 2. (a) IR-corrected Tafel plots (10 mV/s) of the ORR at dense LSM (0.3 cm^2) and LSM-YSZ composite (0.04 cm^2) electrodes at 800 °C in air (dashed lines indicate the best-fit line from which α was obtained). (b) Allen−Hickling plot (eq 4) at 10 mV/s for the ORR at dense LSM (0.30 cm^2) and LSM-YSZ composite (0.04 cm^2) electrodes at 800 °C in air (dashed lines indicate the best-fit line from which α was obtained).

located throughout the porous structure. In collecting our experimental data, we ensured that all three-electrode half-cell geometry issues[15−17] were taken into account and that any uncompensated series resistance (IR) or bulk transport limitations were not influencing our results. It is then seen that the first electron-transfer step is rate limiting for the ORR at dense LSM cathodes (Figure 1a), while at porous LSM-YSZ cathodes (Figure 1b), anomalously high Tafel slopes (very low α values of <0.5), which cannot be interpreted using standard kinetic or adsorption considerations, are obtained.

2. Experimental Methods

The LSM-YSZ composite working electrodes used in our studies (Figure 1b) were fabricated at Versa Power (formerly Global Thermoelectric Inc.), for the purposes of this project, by mixing equal volumes of $(La_{0.8}Sr_{0.2})_{0.98}MnO_3$ (Praxair Ceramics Inc.) with 8 mol % Y_2O_3-doped ZrO_2 (8YSZ, Tosoh) in ethanol and then ball milling. The slurry was screen-printed (using a 325 mesh stainless steel) symmetrically on both sides of a 50 × 50 mm, 0.2 mm thick YSZ plate,[18] covering 40 × 40 mm, resulting in a 10 μm thick layer of composite material. A pure LSM layer (ca. 10 μm thick) was then screen-printed on top of the LSM-YSZ composite layers to serve as a conducting current collector.[18] The YSZ plates were then cut into smaller

TABLE 1: Transfer Coefficients for the Oxygen Reduction Reaction on Dense LSM and Porous LSM-YSZ Composite Electrodes[a]

	transfer coefficient, α						
	dense LSM α_c		dense LSM α_a		porous LSM-YSZ composite α_c		porous LSM-YSZ composite α_a
T (°C)	from TS[c]	from AH[b]	from TS	from AH[c]	from TS	from AH[b]	from AH[b]
550					0.27 ± 0.05	0.21 ± 0.05 (> −0.3 V) 0.59 ± 0.1 (0 to −0.3 V)	0.53 ± 0.05
600	0.67 ± 0.1	0.75 ± 0.1 (> −0.275 V)	0.73 ± 0.1	0.5 ± 0.1	0.34 ± 0.05	0.27 ± 0.05	0.64 ± 0.05
650	0.55 ± 0.05	0.55 (> −0.275 V) 0.7 ± 0.1 (0 to −0.25 V)	1.0 ± 0.05	0.96 ± 0.05	0.34 ± 0.05	0.37 ± 0.05 0.66 ± 0.1 (0 to −0.28 V)	
700	0.55 ± 0.05	0.55 (> −0.275 V) 0.7 ± 0.1 (0 to −0.25 V)	1.0 ± 0.05	0.96 ± 0.05	0.24 ± 0.05	0.26 ± 0.05 0.64 ± 0.1 (−0.2 to −0.38 V)	0.8 ± 0.05
750	0.55 ± 0.05	0.55 (> −0.275 V) 0.7 ± 0.1 (0 to −0.25 V)	1.0 ± 0.05	0.96 ± 0.05	0.25 ± 0.05	0.32 ± 0.05	0.67 ± 0.05
800	0.52 ± 0.05	0.58 ± 0.05 (> −0.275 V)	0.84 ± 0.05	0.89 ± 0.05	0.24 ± 0.05	0.21 ± 0.05 (> −0.3 V) 0.58 ± 0.1 (−0.1 to −0.3 V)	0.61 ± 0.05

[a] Measured from IR-corrected i/η data at 10 mV/s at the overpotentials indicated, all in nonflowing air. [b] Tafel Slope (TS) and Allen−Hickling (AH) method.[13]

rectangular pieces, providing an electrode area of 3 to 20 mm^2, followed by sintering in air at 1100 °C for 2 h. The two sides later served as the working (WE) and counter (CE) electrodes.

Dense LSM electrodes (Figure 1a) were prepared at the National Research Council in Ottawa using a custom-designed Sputter Deposition system with 2" Magnetron Sputter Guns (Torr International). A $(La_{0.8}Sr_{0.2})_{0.98}MnO_3$ target (99.9% purity, Praxair Ceramics Inc.) was sputtered onto a densified 12 mm × 12 mm × 200 μm thick YSZ plate, forming an ∼80 nm thick LSM film through a mask. The pressure of Ar during deposition was 5 mTorr, and the LSM films were deposited at an Ar:O_2 gas flow ratio of 8:2. Sputtering was performed at 4 W/cm^2 RF power and at a 90 mm distance between the substrate, heated to 500 °C by halogen lamps. The samples were then postannealed in O_2 at 800 °C for 1 h. The electrical conductivity of the LSM thin films, measured on sapphire using the Van der Pauw method, was 230 S/cm at 800 °C in air. The dense LSM film then served as the WE, whereas Pt paste (Ferro 4082), attached symmetrically on the opposite side of the electrolyte, served as the CE.

For both the composite LSM-YSZ and dense LSM studies, Pt paste (Ferro 4082) was applied to the YSZ on the same side as the WE to serve as the reference electrode (RE), placed 2 to 5 mm from the WE [18] to prevent electrode geometry artifacts.[19] Pt gauze, attached to a Pt wire, was then press-contacted to each of the electrodes with the aid of a spring-loaded ceramic cap, thus serving as the current collector.

Half-cell experiments, involving air or oxygen (pO_2 ranging from 0.002 to 1 atm), were carried out over temperatures ranging from 600 to 900 °C in a tube furnace (Lindberg). Cyclic voltammetry (CV) measurements (1 to 100 mV/s) were performed using an EG&G PARC 273 potentiostat or a Solartron 1287 interface, with control and data collection handled by Corrware software (version 2.7a). The IR drop, originating from the electrolyte and lead/contact resistances, was compensated for by post factum correction of the CVs, using the series resistance obtained from electrochemical impedance spectroscopy (EIS) data, to establish the resistance-free I/E characteristics. For the EIS analysis, a Solartron 1255 Frequency Response Analyzer was coupled with the potentiostat. The frequency range employed was 0.1 Hz to 500 kHz, and the measurements were made between 0 and −0.4 V dc bias vs the OCP or vs the Pt RE, using a perturbation amplitude of 10 mV rms. EIS data collection and fitting analyses were controlled with commercial software (ZVIEW and ZPLOT, version 2.7). All reported current densities are given vs the geometric area of the electrode, and all potentials are referenced against the Pt pseudo RE, exposed to the same pO_2 atmosphere as the WE.

3. Results and Discussion

3.1. Determination of Transfer Coefficients for ORR on Dense and Porous LSM-based Cathodes. Figure 2a shows the raw and IR-corrected oxygen reduction (ORR) Tafel data at dense LSM and composite LSM-YSZ cathode materials, all at 800 °C. The potential was also extended to positive overpotentials to examine the oxygen evolution (OER) activity. Consistent with what is seen at all temperatures, Figure 2a shows that the ORR activity at the composite electrode is much greater than that at the dense, single-phase LSM electrode, due to its significantly larger tpb area (Figure 1). At −0.3 V, for example, the difference in activity is about 200 times.

It should be noted that all of our i/E data were collected using a symmetrically positioned WE and CE, both having a similar electrochemical time constant (RC product, obtained from the EIS data) and hence any geometry-related artifacts in our experiments should be minimal.[15,17] Also, the Tafel data are independent of both the potential sweep rate and the gas flow rate,[18] thus ruling out any transport processes as being rate limiting for the ORR under these experimental conditions, consistent with the absence of any Warburg-like features in our EIS data.[9,20,21]

Using the appropriate potential range for each temperature,[18] the anodic and cathode Tafel slopes (and transfer coefficients) were obtained from the inverse of the slope of the best-fit line through the high-field data points (Figure 2a), using eq 3 for both the dense and composite cathodes. In general, two cathodic Tafel regions can be discerned for the ORR at the dense LSM and the composite LSM-YSZ cathode materials at low and high overpotentials, as shown in Table 1. As well, the Allen−Hickling (AH) analysis (Figure 2b) gives one or two linear regions. The curvature often seen at very low overpotentials in the AH plots arises from the fact that the currents in the anodic and cathodic scans did not always fully overlap (a net current is seen in both scan directions at 0 V), thus preventing the accurate determination of α_c in this potential range.

At the dense LSM, the α_c values (Table 1) are found to be quite close to 0.5 (± 0.05) at high overpotentials. At overpotentials less than −0.25 to −0.3 V, the AH analysis sometimes revealed a second Tafel region, with an α_c value of close to 0.7 (±0.1), perhaps indicating a transition region over which α_c is

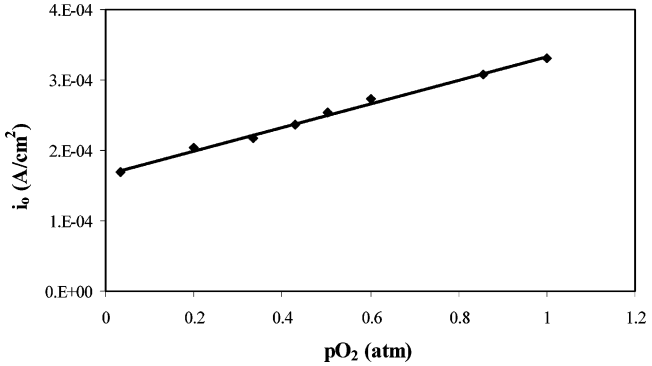

Figure 3. Dependence of i_o on pO_2 (0.03 to 1 atm) during ORR at a dense LSM cathode (0.03 cm^2) on a YSZ disk at 800 °C.

changing from 1 (at still lower overpotentials) to 0.5. Notably, α_a for the oxygen evolution reaction (OER) remained at ~1 (±0.1) at all anodic overpotentials at 650−800 °C, as seen by using either the TS or AH analysis methods.

In comparison, for the porous LSM-YSZ composite electrodes (Table 1), α_a for the OER is between 0.5 and 0.8 for temperatures ranging between 550 and 800 °C, using both the AH and TS methods, quite different from the situation at dense LSM (where α_a was consistently close to 1). For the ORR, Table 1 clearly shows some unexpected results. The α_c values at high overpotentials, essentially at all temperatures, are very low, that is, close to 0.25 (±0.05). In a few cases, an α_c value of ca. 0.5 (±0.1) is seen at lower overpotentials, although curvature in the data generally precludes a more accurate estimation of α_c under these conditions.

Overall, Table 1 shows that α_a is generally larger than α_c for the ORR at either dense LSM or the porous composite materials, especially at higher overpotentials. This shows that the OER is a more rapid reaction than the relatively sluggish ORR, similar to the case under low-temperature aqueous conditions.[22] A second important conclusion is that α_c values of <0.5 are seen for the ORR at the porous composite cathodes, especially at higher overpotentials. Assuming that the symmetry factor $\beta = 0.5$, as is commonly the case, α values of less than 0.5 cannot be explained for simple electron-transfer reactions.[10] However, it has been suggested that β may change when very high overpotentials are applied.[23] Also, it has been proposed that nonuniform current or potential distributions in porous electrodes,[24−26] or the presence of semiconducting layers at the electrode/electrolyte interface,[27,28] can lead to anomalously low α values (<0.5). Another common explanation for the unexpectedly low α values is that the electrochemical reaction involves adsorbed species which obey potential dependent isotherms.[29] It is this latter explanation that is examined closely in this paper (see section 3.3).

3.2. O_2 Reaction Order at LSM-based Cathodes. The activity of the ORR at the dense LSM cathode in pO_2 environments from 0.03 to 1 atm gave a reaction order with respect to O_2, m_{O2}, of ~1 (Figure 3), whereas at the porous LSM-YSZ composite electrodes, m_{O2} was consistently ~0.5 (Figure 4) at all temperatures. This was true whether the reaction order was obtained from the i_o values (using either TS or AH analyses) or from the current measured at various overpotentials. The literature has reported a range of m_{O2} values for the ORR at LSM-derived cathodes. Van Herle et al.'s[30] EIS data on porous LSM gave a m_{O2} of 0.53 at 700 to 900 °C at 10^{-4} to 1 atm pO_2, which was attributed to the adsorption of atomic oxygen at the tpb or at other active surface sites. A m_{O2} value of 1/6, seen for the ORR at dense LSM, was attributed to the

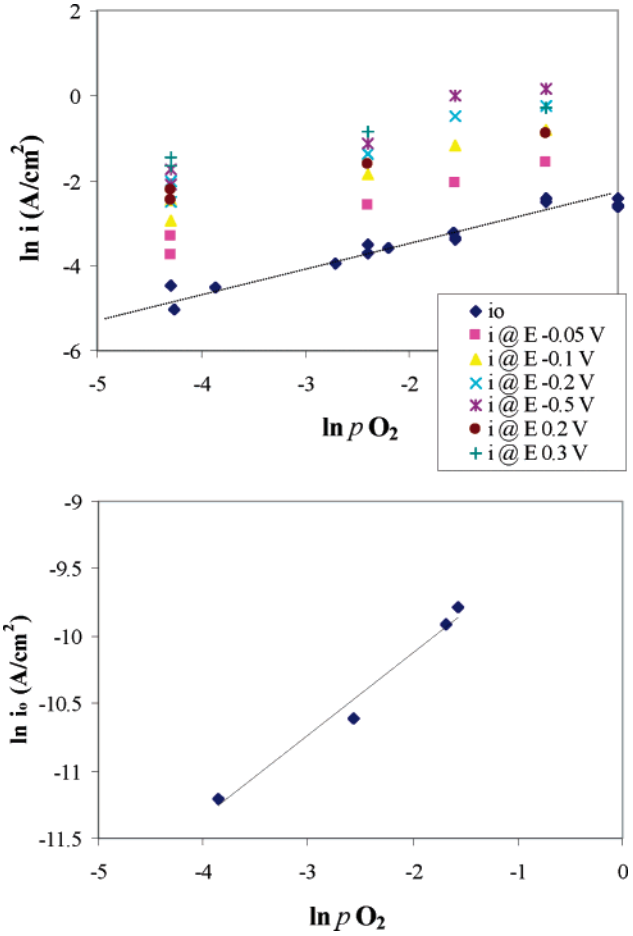

Figure 4. (a) Dependence of current on pO_2 (0.01 to 1 atm) at (◆) i_o, (■) −0.05 V, (▲) −0.1 V, (×) −0.2 V, (*) −0.5 V, (●) 0.2 V, and (+) 0.3 V, during ORR at a porous LSM-YSZ electrode (0.04 cm^2) on a YSZ disk at 800 °C. (b) Dependence of i_o on pO_2 (0.01 to 1 atm) during ORR at a porous LSM-YSZ electrode (0.04 cm^2) on a YSZ disk at 600 °C.

adsorption and then dissociation of O_2 to $2O_{ads}$, which was suggested to be the rds. m_{O2} values of 0.25 and −0.25 at low pO_2 (low surface coverage, θ, ~ 0) and high pO_2 (θ ~ 1) values, respectively, were also reported by Wang and Norwick.[31] Takeda[32] reported a m_{O2} value of 0.75 and attributed this to a rds involving molecular oxygen and atomic oxygen (probably dissociation of the former), whereas a m_{O2} of 0.25 was thought to be due to surface diffusion of O^- along the LSM surface to the tpb.[33] Our analysis below is based on the data obtained at dense and porous LSM-based cathodes and shown in Figures 3 and 4.

3.3. Possible Mechanisms for the Oxygen Reduction Reaction (ORR) at LSM Cathodes. There is no general agreement in the literature regarding the exact mechanism of the ORR at LSM-based cathodes under SOFC conditions.[9,34−38] The overall reaction, where $V_{\ddot{o}}$ is an oxide anion vacancy and O_o^x is an oxygen ion in the vacancy site of LSM, is

$$O_2 + 2V_{\ddot{o}} + 4e^- \rightarrow 2O_o^x \qquad (5)$$

In the present work, four possible mechanistic pathways (A−D) for the reduction of O_2 to O^{2-}, which encompass the majority of the suggested ORR pathways in the published literature, are shown in Figure 5. The most commonly encountered one[39] is very similar to mechanism A but does not include steps 3 and 5.

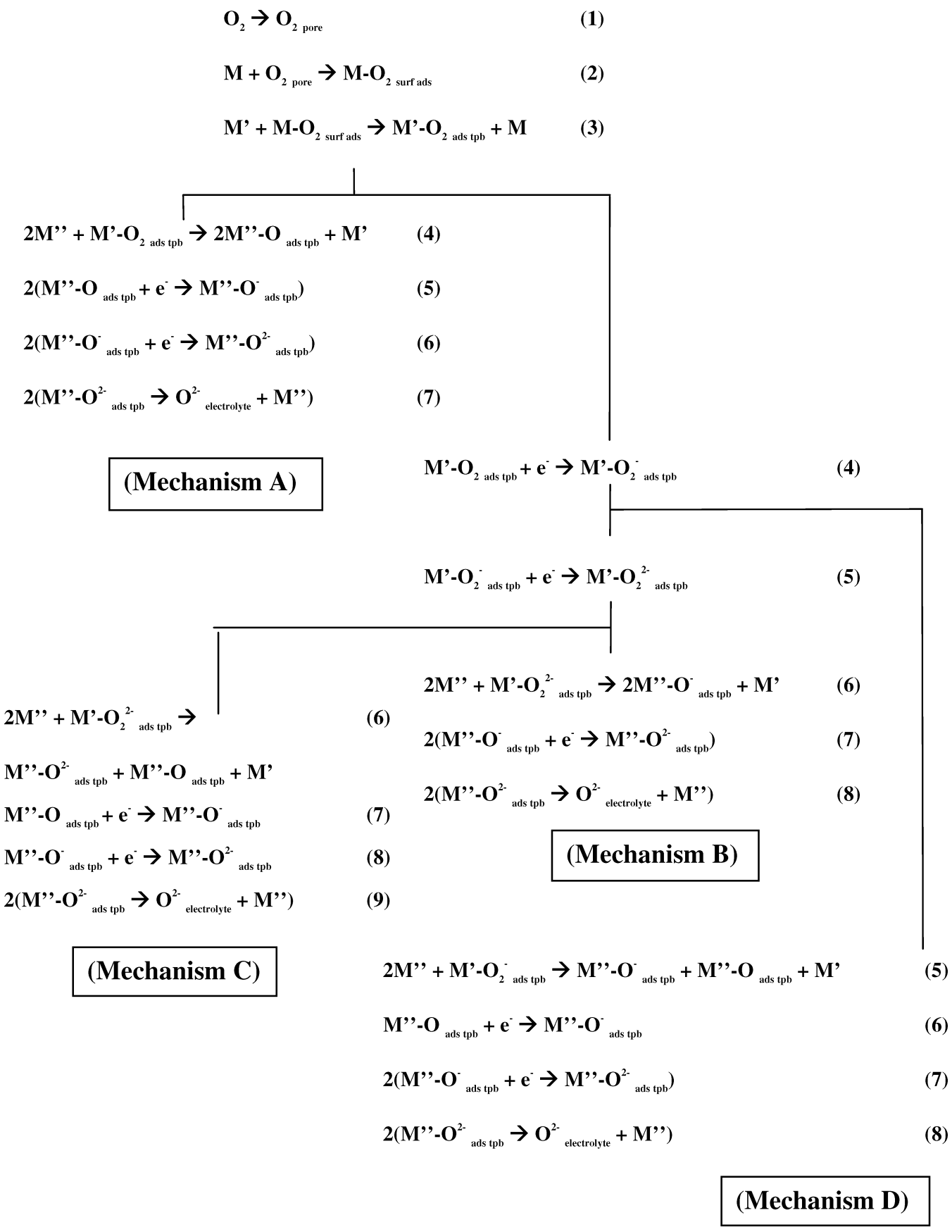

Figure 5. Four oxygen reduction mechanisms considered in this work.

A detailed derivation of the rate equations, r_x (where x denotes the rds) for mechanism A (Figure 5), assuming first that Langmuir conditions apply, and then that adsorbed species obey the Temkin isotherm, is provided below. In terms of mechanisms B to D, the same approaches have been used but only the predicted Tafel slopes and α values, as well as the reaction order, m_{O2}, will be given. In carrying out these calculations, the following assumptions were made.

(a) LSM is a very good electronic conductor with almost negligible ionic conductivity,[40,41] and its ionic and electronic conductivity are independent of potential.

(b) The activity of LSM toward the ORR is highest at the tpb, and the number of active sites at the tpb is independent of time, temperature, η, and pO_2.

(c) When a particular reaction step is rate determining, its i_o is <0.1 that of other reaction steps,[10] so that the other steps can be assumed to be at pseudo-steady-state.

(d) The cathode layers are uniform in structure and thickness and exhibit homogeneous reactivity. While some sites may be more reactive than others in the case of Temkin conditions, only one mechanistic pathway is limiting the ORR at all times.

Through the use of these assumptions, either Langmuir or Temkin adsorption isotherms are assumed to apply to the ORR at dense and porous LSM-based cathodes, to interpret the transfer coefficients obtained (Table 1). Under Temkin conditions,[10,42] surface heterogeneities are considered to be present, with the heat of adsorption becoming linearly less exothermic with increasing surface coverage, θ, of the adsorbed species.[10] In general, the Temkin approach can be used for intermediate surface coverages between $0.2 < \theta < 0.8$, while at $\theta \sim 1$ or ~ 0, the Temkin model reduces to the Langmuir model. The development of the rate expressions will be shown below only for mechanism A, where r_x is the rate of the reaction, k_x is the rate constant, and K_x is the equilibrium constant for step x.

3.3.1. Langmuir Conditions (derivations for mechanism A only are shown here). Initially, it is assumed in mechanism A (Figure 5) that all adsorbed species obey the Langmuir isotherm, where M represents all of the unoccupied adsorption sites on the electrode surface and M′ and M″ represent two different unoccupied adsorption sites at the tpb, for example, M′ for adsorbed O_2 (but not for O) and M″ for adsorbed O (but not O_2). Reactions 1−3 (Figure 5) can be combined, giving reaction 1′. If any of these reactions were the rds, then Tafel behavior would not have been observed, and therefore, this can be ruled out for the ORR at LSM-based cathodes.

$$M' + O_2 \rightarrow M'-O_{2\ ads,tpb'} \tag{1'}$$

Assuming that chemical step 4 (Figure 5), that is, the dissociation of O_2 to 2O, is rate limiting, reaction 1′ can be assumed to be at equilibrium and thus $K_{1'}$ and r_4 can be derived, assuming Langmuir conditions

$$K_{1'} = \frac{k_{-1}}{k_{1'}} = \frac{\theta_{O_2\,tpb,ads}}{[O_2](1 - \theta_{O_2\ tpb,ads})} \tag{6}$$

$$\theta_{O_2\ tpb,ads} = \frac{K_{1'}[O_2]}{1 + K_{1'}[O_2]} \tag{7}$$

$$r_4 = k_4\theta_{O_2\,tpb,ads}(1 - \theta_{tpb,ads}) \tag{8}$$

and assuming that $\theta_{O\ tpb,ads} \ll 1$ such that $(1 - \theta_{O\ tpb,ads}) \approx 1$, then, at high $[O_2]$, when $K_{1'}[O_2] \gg 1$

$$r_4 = k_4 \tag{9}$$

while at low $[O_2]$, when $K_{1'}[O_2] \ll 1$

$$r_4 = k_4K_{1'}[O_2] \tag{10}$$

Up to this point, a potential dependence of the reaction has not yet been encountered. However, when reaction 5, the first electron-transfer step, is assumed to be rate limiting

$$K_4 = \frac{k_{-4}}{k_4} = \frac{\theta_{Otpb,ads}{}^2(1 - \theta_{O_2tpb,ads})}{\theta_{O_2tpb,ads}(1 - \theta_{Otpb,ads})^2} \tag{11}$$

and assuming that $\theta_{O_2tpb,abs} \ll 1$ such that $(1 - \theta_{O_2tpb,abs}) \approx 1$

$$\theta_o = \frac{(K_4\theta_{O_2})^{1/2}}{1 + (K_4\theta_{O_2})^{1/2}} \tag{12}$$

$$r_5 = k_5\theta_{O\ tpb,ads}e^{-\beta_5F\eta/RT} \tag{13}$$

Therefore, at high $[O_2]$

$$r_5 = k_5K_{1'}K_4[O_2]e^{-(1+\beta_5)F\eta/RT} \tag{14}$$

and at low $[O_2]$, where $\theta_{O_2} \sim K_{1'}[O_2]$ and $K_{1'}K_4[O_2] \ll 1$, the rate of the process with reaction 5 as slow is

$$r_5 = k_5(K_{1'}K_4)^{1/2}[O_2]^{1/2}e^{-\beta_5F\eta/RT} \tag{15}$$

The same procedure as shown above (eqs 6−15) were followed for reactions 6 and 7 as rate limiting, as well for mechanisms B to D, assuming that Langmuir adsorption conditions pertain to all adsorbed species. Tables 2−5 summarize the final rate equations, as well as the α values (assuming $\beta = 0.5$) and the O_2 reaction order predicted for each step as rate determining for all four mechanisms. It can be seen that α generally increases (Tafel slope decreases) as the rds moves further down the series of reaction steps. Also, the smallest α value is 0.5, regardless of the rate-limiting step. This indicates that the maximum Tafel slope obtainable at 25 °C is 120 mV and at 800 °C is 430 mV (assuming $\beta = 0.5$).[18] For any rate-limiting step prior to the first electron-transfer step, $\alpha = 0$ and the Tafel slope approaches ∞, often described as mass transfer limited.

Table 1 shows that the ORR at dense LSM cathodes at temperatures between 650 and 800 °C gives α_c values of 0.5 (±0.05) at high overpotentials, with some evidence of a higher α_c (0.7 or higher) at low overpotentials. Figure 3 shows that a m_{O2} of 1 is seen from 0.03 to 1 atm O_2 at dense LSM. The only mechanism that is consistent with these results is mechanism D (Table 5), suggesting that reaction 5 is slow initially and that reaction 4 becomes rate limiting at higher overpotentials.

In the case of the ORR at the porous LSM-YSZ cathodes, the α_c value of 0.25 (±0.05), observed over a wide range of overpotentials (Table 1), does not arise for any of the mechanisms in Table 3. It could be argued that the low α_c value of ∼0.25 is the result of a β_c value of 0.25. However, β_a would then be 0.75 (if the oxidation and reduction reactions have the same mechanism), which would lead to an α_a value of 3.75 or 1.75, if n/ν is 4 or 2, respectively, neither of which are seen in this work (Table 1). Also, it would not make sense that $\beta_c = 0.25$ for the ORR only at the LSM/YSZ interface in a porous composite structure but would be 0.5 at the identical interface in the dense cathode deposited on YSZ.

A more likely explanation for the low α_c value of 0.25 (Table 1) is that the Tafel slopes at the porous LSM-YSZ cathodes have been doubled (α values halved) as a result of a distribution of potential within the porous matrix, also described in terms of a transmission line effect.[24,25,43] If this is the case, then the α_c values seen at dense LSM (0.5 (±0.05) at high overpotentials and ∼0.7 or higher at low overpotentials) will be halved at the

TABLE 2: Predicted α_c, O_2 Dependence, and Rate Equations for the ORR for Mechanism A (Langmuir conditions)

mechanism A	rxn no.	rate equation	α_c	$[O_2]$ order[a]
$M' + O_2 \rightarrow M'-O_{2\ tpb,ads}$	1′	$r_1 = k_1[O_2]$	0	
$M'' + M'-O_{2\ ads,tpb} \rightarrow 2\ M''-O_{\ ads,\ tpb}$	4	$r_4 = k_4 K_3$	0	high $[O_2] \rightarrow 0$
		$r_4 = k_3 K_{1'}[O_2]$	0	low $[O_2] \rightarrow 1$
$2(M''-O_{ads,\ tpb} + e^- \rightarrow M''-O^-_{\ ads,\ tpb})$	5	$r_5 = k_5 K_4^{1/2}/(1 + K_4^{1/2})e^{-\beta_5 F\eta/RT}$	0.5	high $[O_2] \rightarrow 0$
		$r_5 = k_5(K_{1'}K_4)^{1/2}[O_2]^{1/2}e^{-\beta_5 F\eta/RT}$	0.5	low $[O_2] \rightarrow 1/2$
$2(M''-O^-_{ads,\ tpb} + e^- \rightarrow M''-O^{2-}_{ads,\ tpb})$	6	$r_6 = k_6 K_5 K_4^{1/2}/(1 + K_4^{1/2})e^{-(1+\beta_6)F\eta/RT}$	1.5	high $[O_2] \rightarrow 0$
		$r_6 = k_6 K_5(K_{1'}K_4)^{1/2}/[O_2]^{1/2}e^{-(1+\beta_6)F\eta/RT}$	1.5	low $[O_2] \rightarrow 1/2$
$2(M''-O^{2-}_{ads,\ tpb} \rightarrow O^{2-}_{electrolyte})$	7	$r_7 = k_7 K_5 K_6 K_4^{1/2}/(1 + K_4^{1/2})e^{-2\beta_7 F\eta/RT}$	2	high $[O_2] \rightarrow 0$
		$r_7 = k_7 K_5 K_6(K_{1'}K_4)^{1/2}[O_2]^{1/2}e^{-2\beta_7 F\eta/RT}$	2	low $[O_2] \rightarrow 1/2$

[a] The meaning of high vs low $[O_2]$ depends on the value of K_x.

TABLE 3: Predicted α_c, O_2 Dependence, and Rate Equations for the ORR for Mechanism B (Langmuir conditions)

mechanism B	rxn no.	rate equation	α_c	$[O_2]$ order[a]
$M' + O_2 \rightarrow M'-O_{2\ tpb,\ ads}$	1′	$r_1 = k_1[O_2]$	0	
$M'-O_{2\ ads,\ tpb} + e^- \rightarrow M'-O_2^-{}_{ads,\ tpb}$	4	$r_4 = k_4 e^{-\beta_4 F\eta/RT}$	0.5	high $[O_2] \rightarrow 0$
		$r_4 = k_4 K_{1'}[O_2]e^{-\beta_4 F\eta/RT}$	0.5	low $[O_2] \rightarrow 1$
$M'-O_2^-{}_{ads\ ,tpb} + e^- \rightarrow M'-O_2^{2-}{}_{ads,\ tpb}$	5	$r_5 = k_5 K_4 e^{-(1+\beta_5)F\eta/RT}$	1.5	high $[O_2] \rightarrow 0$
		$r_5 = k_5 K_{1'}K_4[O_2]e^{-(1+\beta_5)F\eta/RT}$	1.5	low $[O_2] \rightarrow 1$
$2M'' + M'-O_2^{2-}{}_{ads,\ tpb} \rightarrow 2M''-O^-_{ads\ ,tpb} + M'$	6	$r_6 = k_6 K_5 K_4 e^{-2F\eta/RT}$	2	high $[O_2] \rightarrow 0$
		$r_6 = k_6 K_{1'}K_4 K_4^{1/2}/[O_2]e^{-2F\eta/RT}$	2	low $[O_2] \rightarrow 1$
$2(M''-O^-_{ads\ ,tpb} + e^- \rightarrow M''-O^{2-}{}_{ads,tpb})$	7	$r_7 = k_7(K_4 K_5 K_6)^{1/2}e^{-(1+\beta_7)F\eta/RT}$	1.5	high $[O_2] \rightarrow 0$
		$r_7 = k_7(K_{1'}K_4 K_5 K_6)^{1/2}[O_2]^{1/2}e^{-(1+\beta_7)F\eta/RT}$	1.5	low $[O_2] \rightarrow 1/2$
$2(M''\text{-}O^{2-}{}_{ads\ tpb} \rightarrow O^{2-}{}_{electrolyte} + M'')$	8	$r_8 = k_8 K_7(K_4 K_5 K_6)^{1/2}e^{-2\beta_8 F\eta/RT}$	2	high $[O_2] \rightarrow 0$
		$r_8 = k_8 K_7(K_{1'}K_4 K_5 K_6)^{1/2}[O_2]^{1/2}e^{-2\beta_8 F\eta/RT}$	2	low $[O_2] \rightarrow 1/2$

[a] The meaning of high vs low $[O_2]$ depends on the value of K_x.

TABLE 4: Predicted α_c, O_2 Dependence, and Rate Equations for the ORR for Mechanism C (Langmuir conditions)

mechanism C	rxn no.	rate equation	α_c	$[O_2]$ order[a]
$M' + O_2 \rightarrow M'-O_{2\ tpb,ads}$	1′	$r_1 = k_1[O_2]$	0	
$M'-O_{2ads,\ tpb} + e^- \rightarrow M'-O_2^-{}_{ads,\ tpb}$	4	$r_4 = k_4 e^{-\beta_4 F\eta/RT}$	0.5	high $[O_2] \rightarrow 0$
		$r_4 = k_4 K_{1'}[O_2]e^{-\beta_4 F\eta/RT}$	0.5	low $[O_2] \rightarrow 1$
$M'-O_2^-{}_{ads,\ tpb} + e^- \rightarrow M'-O_2^{2-}{}_{ads,\ tpb}$	5	$r_5 = k_5 K_4 e^{-(1+\beta_5)F\eta/RT}$	1.5	high $[O_2] \rightarrow 0$
		$r_5 = k_5 K_{1'}K_4[O_2]e^{-(1+\beta_5)F\eta/RT}$	1.5	low $[O_2] \rightarrow 1$
$2M'' + M'-O_2^{2-}{}_{ads,\ tpb} \rightarrow M''-O^{2-}{}_{ads\ ,tpb} + M''-O_{ads,\ tpb} + M'$	6	$r_6 = k_6 K_4 K_5 e^{-2F\eta/RT}$	2	high $[O_2] \rightarrow 0$
		$r_6 = k_6 K_{1'}K_4 K_5[O_2]e^{-2F\eta/RT}$	2	low $[O_2] \rightarrow 1$
$M''-O_{ads,\ tpb} + e^- \rightarrow M''-O^-_{ads,tpb}$	7	$r_7 = k_7(K_4 K_5 K_6)^{1/2}e^{-(1+\beta_7)F\eta/RT}$	1.5	high $[O_2] \rightarrow 0$
		$r_7 = k_7(K_{1'}K_4 K_5 K_6)^{1/2}[O_2]^{1/2}e^{-(1+\beta_7)F\eta/RT}$	1.5	low $[O_2] \rightarrow 1/2$
$M''-O^-_{ads,\ tpb} + e^- \rightarrow M''-O^{2-}_{ads,\ tpb}$	8	$r_8 = k_8 K_7(K_4 K_5 K_6)^{1/2}e^{-(2+\beta_8)F\eta/RT}$	2.5	high $[O_2] \rightarrow 0$
		$r_8 = k_8 K_7(K_{1'}K_4 K_5 K_6)^{1/2}[O_2]^{1/2}e^{-(2+\beta_8)F\eta/RT}$	2.5	low $[O_2] \rightarrow 1/2$
$2(M''-O^{2-}_{ads,\ tpb} \rightarrow O^{2-}_{electrolyte} + M'')$	9	$r_9 = k_9 K_7 K_8(K_4 K_5 K_6)^{1/2}e^{-3F\eta/RT}$	3	high $[O_2] \rightarrow 0$
		$r_9 = k_9 K_7 K_8(K_{1'}K_4 K_5 K_6)^{1/2}[O_2]^{1/2}e^{-3F\eta/RT}$	3	low $[O_2] \rightarrow 1/2$

[a] The meaning of high vs low $[O_2]$ depends on the value of K_x.

TABLE 5: Predicted α_c, O_2 Dependence, and Rate Equations for the ORR for Mechanism D (Langmuir conditions)

mechanism D	rxn no.	rate equation	α_c	$[O_2]$ order[a]
$M' + O_2 \rightarrow M'-O_{2\ tpb,ads}$	1′	$r_1 = k_1[O_2]$	0	
$M'-O_{2\ ads\ ,tpb} + e^- \rightarrow M'-O_2^-{}_{ads,\ tpb}$	4	$r_4 = k_4 e^{-\beta_4 F\eta/RT}$	0.5	high $[O_2] \rightarrow 0$
		$r_4 = k_4 K_{1'}[O_2]e^{-\beta_4 F\eta/RT}$	0.5	low $[O_2] \rightarrow 1$
$2M'' + M'-O_2^-{}_{ads,\ tpb} \rightarrow M''-O^-_{ads,tpb} + M''-O_{ads,tpb} + M'$	5	$r_5 = k_5 K_4 e^{-F\eta/RT}$	1	high $[O_2] \rightarrow 0$
		$r_5 = k_5 K_{1'}K_4[O_2]e^{-F\eta/RT}$	1	low $[O_2] \rightarrow 1$
$M''-O_{ads,tpb} + e^- \rightarrow M''-O^-_{ads,tpb}$	6	$r_6 = k_6(K_4 K_5)^{1/2}e^{-F\eta/RT}$	1	high $[O_2] \rightarrow 0$
		$r_6 = k_6(K_{1'}K_4 K_5)^{1/2}[O_2]^{1/2}e^{-F\eta/RT}$	1	low $[O_2] \rightarrow 1/2$
$2(M''-O^-_{ads,tpb} + e^- \rightarrow M''-O^{2-}_{ads,tpb})$	7	$r_7 = k_7 K_6(K_4 K_5)^{1/2}e^{-2F\eta/RT}$	2	high $[O_2] \rightarrow 0$
		$r_7 = k_7 K_6(K_{1'}K_4 K_5)^{1/2}[O_2]^{1/2}e^{-2F\eta/RT}$	2	low $[O_2] \rightarrow 1/2$
$2(M''-O^{2-}_{ads,tpb} \rightarrow O^{2-}_{electrolyte} + M'')$	8	$r_8 = k_8 K_6 K_7(K_4 K_5)^{1/2}e^{-2.5F\eta/RT}$	2.5	high $[O_2] \rightarrow 0$
		$r_8 = k_8 K_6 K_7(K_{1'}K_4 K_5)^{1/2}[O_2]^{1/2}e^{-2.5F\eta/RT}$	2.5	low $[O_2] \rightarrow 1/2$

[a] The meaning of high vs low $[O_2]$ depends on the value of K_x.

porous counterparts, leading to α_c values of 0.25 ($\pm$0.05) and $\sim$0.35, respectively. This is indeed observed for the porous LSM-YSZ composites, suggesting that the ORR follows mechanism D at these cathodes as well, as expected.

Notably, Figure 4 shows that the m_{O2} value is 0.5 at the porous cathode materials (vs 1.0 at dense LSM), which is inconsistent with any of the predictions of mechanisms A to D (Table 5). However, it has been shown[26] that if a Tafel slope is doubled (α is halved) as a result of distributed potentials within a porous matrix and if this arises from ionic migration limitations, then the reaction orders can also be expected to halve in value. This is completely consistent with what is seen in the present work, that is, m_{O2} is 1.0 for the ORR at the dense (nonporous) LSM-YSZ interface and 0.5 at its porous composite LSM-YSZ analogue.

It is also known that the value of Tafel slopes can be greatly influenced by the operative adsorption isotherm. Therefore, the Temkin isotherm was examined here to determine if the low

α_c value of 0.25 would arise through this means and also to gain further insight into the ORR mechanism at LSM-based cathodes under SOFC conditions.

3.3.2. Temkin Conditions. Commencing with mechanism A and assuming that all adsorbed species follow Temkin adsorption conditions, assuming that reaction (1′) is rate limiting, the rate expression for the forward (eq 16) and the reverse reaction (eq 17) can be represented by

$$r_1 = k_{1'}(1 - \theta_{O_2})[O_2]e^{-\gamma O_2 f\theta O_2} \quad (16)$$

$$r_{-1'} = k_{-1'}\theta_{O_2}e^{(1-\gamma O_2)f\theta O_2} \quad (17)$$

where γ is a proportionality constant, having values of $0 < \gamma \leq 1$. While the magnitude of γ depends on the form of the energy barrier for the activation-controlled process, it is usually assumed to be 0.5.[44] f is defined as the rate of change of the apparent standard free energy of adsorption with surface coverage.[44] Values of f from 10 to 40 have been reported for the gas-phase adsorption of H_2 and O_2, while f values of 3 to 10 were found for the electrochemical adsorption of formate radicals from formic acid solutions.[44] Assuming that the concentration of the adsorbed intermediates, θ, affects the rates of these reactions primarily through the exponential terms, such that the preexponential θ terms are very small, $r_{1'}$ and $r_{-1'}$ can also be represented as

$$r_{1'} \cong k_{1'}[O_2]e^{-\gamma O_2 f\theta O_2} \quad (18)$$

$$r_{-1'} = k_{-1'}e^{(1-\gamma O_2)f\theta O_2} \quad (19)$$

The quasi-equilibrium assumption for step 1′ is used to simplify the rate equation. When $r_{1'} = r_{-1'}$

$$K_{1'} = \frac{k_{-1'}}{k_{1'}} = \frac{\theta_{O_2}e^{(1-\gamma O_2)f\theta O_2}}{[O_2](1 - \theta_{O_2})e^{-\gamma O_2 f\theta O_2}} \quad (20)$$

which can be simplified to

$$K_{1'} \cong \frac{e^{(1-\gamma O_2)f\theta O_2}}{[O_2]e^{-\gamma O_2 f\theta O_2}} \quad (21)$$

such that

$$f\theta_{O_2} \cong \ln(K_{1'}[O_2]) \quad (22)$$

Thus, for step 1′ as the rds

$$r_{1'} = k_{1'}[O_2](1 - \theta_{O_2})e^{-\gamma O_2 f\theta O_2} \quad (23)$$

$$r_{1'} = k_{1'}[O_2]e^{-\gamma O_2 \ln(K_{1'}[O_2])} \quad (24)$$

$$r_{1'} = k_{1'}K_{1'}{}^{-\gamma O_2}[O_2]^{1-\gamma O_2} \quad (25)$$

The above treatment assumes that the adsorption of O_2 to the surface of the catalysts is an activated process (but potential independent). On the other hand, for the case when O_2 simply approaches the active tpb and physically adsorbs, requiring no energy of activation,[45,46] the rate equation for step 1′ is further simplified to

$$r_{1'} \cong k_{1'}[O_2]e^{f\theta O_2} \cong k_{1'}K_{1'}{}^{-1/2}[O_2]^{1/2} \quad (26)$$

where

$$K_{1'} \cong \frac{e^{f\theta O_2}}{[O_2]e^{-f\theta O_2}} \quad (27)$$

and

$$f\theta_{O_2} \cong \frac{1}{2}\ln(K_{1'}[O_2]) \quad (28)$$

Assuming $\gamma = 0.5$, the rate equation, $r_{1'}$, representing the activated adsorption of O_2 at the tpb sites (eq 25), is essentially the same as the rate equation for nonactivated adsorption (eq 26), which suggests that $r_{1'}$, derived for nonactivated adsorption, is a simplified subset of $r_{1'}$. Thus, the derivation of the rate equations for steps 4−7 as the slow steps in mechanism A (Figure 5) assumes activated O_2 adsorption for step 1′.

For step 4 as the rds

$$r_4 = k_4\theta_{O_2}(1 - \theta_O)^2e^{(1-\gamma O_2)f\theta O_2}e^{-2\gamma Of\theta_O} \cong k_4e^{(1-\gamma O_2)f\theta O_2}e^{-2\gamma Of\theta_O} \quad (29)$$

This step involves the dissociation of O_2 to two O adatoms on the surface, and to simplify the subsequent treatment, it is assumed that $\theta_{O2} = {}^1/_2\theta_O$. This simplifies r_4, where $f\theta_{O2} \cong \ln(K_{1'}[O_2])$

$$r_4 \cong k_4e^{(1-\gamma O_2-4\gamma O)f\theta_{O2}} \cong k_4(K_{1'}[O_2])^{(1-\gamma O_2-4\gamma O)} \quad (30)$$

For step 5 as the rds

$$r_5 = k_5\theta_Oe^{(1-\gamma O)f\theta_{O-}}e^{-\gamma O^- f\theta_{O-}}e^{-\beta_5 F\eta/RT} \quad (31)$$

This step implies that the reduction of adsorbed O to adsorbed O^- occurs on the same catalyst site and thus the total coverage remains unchanged, that is, $\theta_O = \theta_{O-}$, giving

$$r_5 = k_5\theta_Oe^{(1-\gamma O-\gamma O^-)f\theta_O}e^{-\beta_5 F\eta/RT} \quad (32)$$

When

$$K_4 = \frac{k_{-4}}{k_4} = \frac{\theta_{O_2}{}^2e^{-\gamma O_2 f\theta O_2}e^{2(1-\gamma O)f\theta_O}}{\theta_{O_2}(1 - \theta_O - \theta_{O_2})e^{(1-\gamma O_2)f\theta O2}e^{-2\gamma Of\theta_O}} \quad (33)$$

such that

$$f\theta_O \cong \frac{1}{2}(\ln K_4 + f\theta_{O_2}) \cong \frac{1}{2}(\ln K_4 + \ln K_{1'}[O_2]) \quad (34)$$

then

$$r_5 \cong k_5(K_{1'}K_4[O_2])^{1/2(1-\gamma O-\gamma O^-)}e^{-\beta_5 F\eta/RT} \quad (35)$$

Through the use of the same approach as above, the resulting equations and predicted α and m_{O2} values for mechanisms A to D (Figure 5), assuming that $\beta_c = 0.5$ and that all of the adsorbed species obey Temkin adsorption conditions, can be found in Tables 6−9. It is seen that none of mechanisms A to D fit the experimental ORR data at either dense or porous LSM cathodes, indicating that the adsorbed species do not obey Temkin conditions. While the α values obtained using the Temkin isotherm are generally smaller for the same rds vs in the Langmuir case, Temkin conditions never give an α_c value smaller than 0.5. For example, steps 6 and 7 of mechanism A

TABLE 6: Predicted α_c, O_2 Dependence, and Rate Equations for the ORR for Mechanism A (Temkin conditions)

mechanism A	rxn no.	rate equation	α_c	$[O_2]$ order[a]
$M' + O_2 \rightarrow M'-O_{2\ tpb,ads}$	1′	$r_{1'} = k_{1'}K_{1'}^{-\gamma O_2}[O_2]^{-\gamma O_2}$ activated ads[b] $r_{1'} = k_{1'}K_1^{-0.5}[O_2]^{-0.5}$ nonactivated ads[b]	0	0.5
$M'' + M'-O_{2\ ads,tpb} \rightarrow 2\ M''-O_{ads,tpb}$	4	$r_4 = k_4(K_{1'}[O_2])^{1-\gamma O_2-4\gamma O}$ (2′) is activated ads	0	−1.5
$2(M''-O_{ads,tpb} + e^- \rightarrow M''-O^-_{\ ads,tpb})$	5	$r_5 = k_5(K_{1'}K_4[O_2])^{1/2(1-\gamma O-\gamma O^-)}e^{-\beta_5 F\eta/RT}$ (2′) activated ads	0.5	0
$2(M''-O^-_{ads,tpb} + e^- \rightarrow M''-O^{2-}_{ads,tpb})$	6	$r_6 = k_6[K_5(K_{1'}K_4[O_2])^{1/2}]^{(1-\gamma O^- -\gamma O^{2-})}e^{-(\beta_6+1-\gamma O^- -\gamma O^{2-})F\eta/RT}$ (2′) activated ads	0.5	0.5
$2(M''-O^{2-}_{ad\ s,tpb} \rightarrow O^{2-}_{\ electrolyte})$	7	$r_7 = k_7[K_5K_6(K_{1'}K_4[O_2])^{1/2}]^{(1-\gamma O^{2-})}e^{-2(1-\gamma O^{2-})F\eta/RT}$ (2′) activated ads	1	0.25

[a] TS and reaction orders given in this table are based on $\gamma = 0.5$. [b] Activated and nonactivated adsorption denotes chemisorbed and physisorbed species, respectively.

TABLE 7: Predicted α_c, O_2 Dependence, and Rate Equations for the ORR for Mechanism B (Temkin conditions)

mechanism B	rxn no.	rate equation	α_c	$[O_2]$ order[a]
$M' + O_2 \rightarrow M'-O_{2\ tpb,ads}$	1′	$r_{1'} = k_{1'}K_{1'}^{-\gamma O_2}[O_2]^{-\gamma O_2}$ activated ads[b] $r_{1'} = k_{1'}K_1^{-0.5}[O_2]^{-0.5}$ nonactivated ads[b]	0	0.5
$M'-O_{2\ ads,tpb} + e^- \rightarrow M'-O_2^-{}_{ads,tpb}$	4	$r_4 = k_4(K_{1'}[O_2])^{1-\gamma O_2-\gamma O_2^-}e^{-\beta_4 F\eta/RT}$ (2′) is activated ads	0.5	0
$M'\text{-}O_2^-{}_{ads,tpb} + e^- \rightarrow M'-O_2^{2-}{}_{ads,tpb}$	5	$r_5 = k_5(K_{1'}K_4[O_2])^{(1-\gamma O_2^- -\gamma O_2^{2-})}e^{-(\beta_5+1-\gamma O^{2-}-\gamma O^{2-}{}_2)F\eta/RT}$ (2′) activated ads	0.5	0
$2M'' + M'-O_2^{2-}{}_{ads,tpb} \rightarrow M''-O^-_{ads,tpb} + M'$	6	$r_6 = k_6(K_{1'}K_4K_5[O_2])^{(1-\gamma O_2{}^{2-}-4\gamma O^-)}e^{-2(1-\gamma O^{2-}{}_2-4\gamma O^-)F\eta/RT}$ (2′) activated ads		
$2(M''-O^-_{ads,tpb} + e^- \rightarrow M''-O^{2-}_{ads,tpb})$	7	$r_7 = k_7(K_{1'}K_4K_5K_6[O_2])^{1/2(1-\gamma O^- -\gamma O^{2-})}e^{-(\beta+1-\gamma O^- -\gamma O^{2-})F\eta/RT}$ (2′) activated ads	0.5	0
$2(M''-O^{2-}_{ads,tpb} \rightarrow O^{2-}_{electrolyte} + M'')$	8	$r_8 = k_8[K_7(K_{1'}K_4K_5K_6[O_2])^{1/2}]^{(1-\gamma O^{2-})}e^{-2(1-\gamma O_2{}^-)F\eta/RT}$ (2′) activated ads	1	0.25

[a] TS and reaction orders given in this table are based on $\gamma = 0.5$. [b] Activated and nonactivated adsorption denotes chemiabsorbed and physisorbed species, respectively.

TABLE 8: Predicted α_c, O_2 Dependence, and Rate Equations for the ORR for Mechanism C (Temkin conditions)

mechanism C	rxn no.	rate equation	α_c	$[O_2]$ order[a]
$M' + O_2 \rightarrow M'-O_{2\ tpb,ads}$	1′	$r_{1'} = k_{1'}K_{1'}^{-\gamma O_2}[O_2]^{-\gamma O_2}$ activated ads[b] $r_{1'} = k_{1'}K_1^{-0.5}[O_2]^{-0.5}$ nonactivated ads[b]	0	0.5
$M'-O_{2\ ads,tpb} + e^- \rightarrow M'-O_2^-{}_{ads,tpb}$	4	$r_4 = k_4(K_{1'}[O_2])^{1-\gamma O_2^- \gamma O_2^-}e^{-\beta_4 F\eta/RT}$ (2′) is activated ads	0.5	0
$M'-O_2^-{}_{ads,tpb} + e^- \rightarrow M'-O_2^{2-}{}_{ads,tpb}$	5	$r_5 = k_5(K_{1'}K_4[O_2])^{(1-\gamma O_2^- -\gamma O_2{}^{2-})}e^{-(\beta_5+1-\gamma O_2^- -\gamma O_2{}^{2-})F\eta/RT}$ (2′) activated ads	0.5	0
$2M'' + M'-O_2^{2-}{}_{ads,tpb} \rightarrow$ $M''-O^{2-}_{ads,tpb} + M''-O_{ads,tpb} + M'$	6	$r_6 = k_6(K_{1'}K_4K_5[O_2])^{(1-\gamma O_2{}^{2-}-\gamma O^{2-}-\gamma O)}e^{-2(1-\gamma O_2{}^{2-}-\gamma O^{2-}-\gamma O)F\eta/RT}$ (2′) activated ads	1	−0.5
$M''-O_{\ ads,tpb} + e^- \rightarrow M''-O^-_{\ ads,tpb}$	7	$r_7 = k_7(K_{1'}K_4K_5K_6K_7^{-1}K_8^{-1}[O_2])^{1/2(1-\gamma O-\gamma O^-)}e^{-\beta_7 F\eta/RT}$ (2′) activated ads	0.5	0
$M''-O^-_{ads,tpb} + e^- \rightarrow M''-O^{2-}_{ads,tpb}$	8	$r_8 = k_8(K_{1'}K_4K_5K_6K_7K_8^{-1}[O_2])^{1/2(1-\gamma O-\gamma O^{2-})}e^{-(\beta_8+1-\gamma O-\gamma O^{2-})F\eta/RT}$ (2′) activated ads	0.5	0
$2(M''-O^{2-}_{ads,tpb} \rightarrow O^{2-}_{electrolyte} + M'')$	9	$r_9 = k_9(K_{1'}K_4K_5K_6K_7K_8^{-1}[O_2])^{1/2(1-\gamma O^{2-})}e^{-2(1-\gamma O^{2-})F\eta/RT}$ (2′) activated ads	1	0.25

[a] TS and reaction orders given in this table are based on $\gamma = 0.5$. [b] Activated and nonactivated adsorption denotes chemisorbed and physisorbed species, respectively.

(Tables 3 and 7) give α_c values of 1.5 and 2, respectively, using the Langmuir approach, and α_c values of 0.5 and 1 for Temkin conditions. Therefore, electrochemically measured α values of <0.5 cannot be explained through the use of these adsorption models.

3.4. Analysis of Oxygen Evolution Data at LSM-based Electrodes. A similar Langmuir and Temkin adsorption analysis was also performed on the oxygen evolution (OER) data, assuming that the OER follows the same steps as shown in Figure 5. Table 10 gives the predicted α_c and α_a values for the ORR and OER, respectively, for mechanism D, assuming that the adsorbed species follow either Langmuir or Temkin conditions and have the same n/ν values.

In the classical Butler−Volmer derivation, assuming microscopic reversibility and ignoring adsorption effects, the sum of α_c and α_a is expected to be n/ν, that is, an integer. However, this is not seen for the experimental ORR data presented in this paper (Table 1). For dense LSM, n/ν is 1.5 at low η and 2 at high η, while for porous composites, n/ν is between 1 and 1.5 at low η and ∼0.75 at high η. This may reflect the fact that Langmuir or Temkin conditions pertain here (Table 10) or that the ORR and OER reactions do not occur via the same

TABLE 9: Predicted α_c, O_2 Dependence, and Rate Equations for the ORR for Mechanism D (Temkin conditions)

mechanism D	rxn no.	rate equation	α_c	$[O_2]$ order[a]
$M' + O_2 \rightarrow M'-O_{2\ tpb,ads}$	1′	$r_{1'} = k_{1'}K_{1'}^{-\gamma_{O_2}}[O_2]^{-\gamma_{O_2}}$ activated ads[b] $r_{1'} = k_{1'}K_1^{-0.5}[O_2]^{-0.5}$ nonactivated ads[b]	0	0.5
$M'-O_{2\ ads,tpb} + e^- \rightarrow M'-O_2^-{}_{ads,tpb}$	4	$r_4 = k_4(K_{1'}[O_2])^{1-\gamma_{O_2}-\gamma_{O_2^-}}e^{-\beta_4 F\eta/RT}$ (1′) is activated ads	0.5	0
$2M'' + M'-O_2^-{}_{ads,tpb} \rightarrow M''-O^-{}_{ads,tpb} + M''-O_{ads,tpb} + M'$	5	$r_5 = k_5(K_{1'}K_4[O_2])^{(1-\gamma_{O_2^-}-\gamma_{O^-}-\gamma_O)}\ e^{-(1-\gamma_{O_2^-}-\gamma_{O^-}-\gamma_O)F\eta/RT}$ (1′) activated ads	0.5	−0.5
$M''-O_{ads,tpb} + e^- \rightarrow M''-O^-{}_{ads,tpb}$	6	$r_6 = k_6(K_{1'}K_4K_5K_6{}^{-1}[O_2])^{1/2(1-\gamma_O-\gamma_{O^-})}e^{(1-\gamma_O-\gamma_{O^-}-\beta_6)F\eta/RT}$ (1′) activated ads	0.5	0
$2(M''-O^-{}_{ads,tpb} + e^- \rightarrow M''-O^{2-}{}_{ads,tpb})$	7	$r_7 = k_7(K_{1'}K_4K_5K_6[O_2])^{1/2(1-\gamma_{O^-}\gamma_{O_2^-})}e^{-(\beta_7+2(1-\gamma_{O^-}-\gamma_{O^{2-}})]F\eta/RT}$ (1′) activated ads	0.5	0
$2(M''-O^{2-}{}_{ads,tpb} \rightarrow O^{2-}{}_{electrolyte} + M'')$	8	$r_8 = k_8[K_7(K_{1'}K_4K_5K_6[O_2])^{1/2}]^{(1-\gamma_{O^{2-}})}e^{-3(1-\gamma_{O^{2-}})]F\eta/RT}$ (1′) activated ads	1	0.25

[a] TS and reaction orders given in this table are based on $\gamma = 0.5$. [b] Activated and nonactivated adsorption denotes chemisorbed and physisorbed species, respectively.

TABLE 10: Predicted α_c, α_a, and n/ν Values for Oxygen Reduction and Evolution, Assuming Microscopic Reversibility of Mechanism A for Both Langmuir or Temkin Adsorption Conditions

		Langmuir			Temkin		
assumed slow step	rxn no.	α_c	α_a[a]	n/ν[b]	α_c	α_a[a]	n/ν[b]
$M' + O_2 \rightarrow M'-O_{2\ tpb,ads}$	1′	0	4	4	0	2	2
$M'-O_{2\ ads,tpb} + e^- \rightarrow M'-O_2^-{}_{ads,tpb}$	4	0.5	3.5	4	0.5	0	0.5
$2M'' + M'-O_2^-{}_{ads,\ tpb} \rightarrow M''-O^-{}_{ads,tpb} + M''-O_{ads,tpb} + M'$	5	1	3	4	0.5	0	0.5
$M''-O_{ads,tpb} + e^- \rightarrow M''-O^-{}_{ads,tpb}$	6	1	1.5	2.5	0.5	0	0.5
$2(M''-O^-{}_{ads,tpb} + e^- \rightarrow M''-O^{2-}{}_{ads,tpb})$	7	2	0.5	2.5	0.5	0	0.5
$2(M''-O^{2-}{}_{ads,tpb} \rightarrow O^{2-}{}_{electrolyte} + M'')$	8	2.5	0	2.5	1	0	1

[a] α_a values are obtained from the derived rate equations. [b] n is assumed to be 4 and ν assumed to be 1 for the ORR and OER.

mechanism. For the porous LSM, it is also possible that $\alpha_c + \alpha_a < n/\nu$ results from a nonuniform potential distribution within the cathode layer.[43]

Other types of adsorption isotherms accounting for lateral interactions between adsorbed species (e.g., Frumkin and Flory−Huggins isotherms),[10,47,48] solvent displacement (Flory−Huggins isotherm), or partial charge transfer of adsorbed molecules and the substrate,[49] have also been examined in the literature for other reactions, normally under aqueous, room-temperature conditions. As expected, these interactions increase the complexity of the rate equations, although the Frumkin isotherm model generally gives similar rate equations to those arising from the Temkin model. Notably, it is likely that these other adsorption models will also not satisfy the condition of n/ν (assuming $n = 4$ and $\nu = 1$) $= \alpha_c + \alpha_a$.

4. Summary

The oxygen reduction reaction (ORR) is one of the key factors limiting the power output of present-day solid oxide fuel cells (SOFCs). To understand this further, the ORR kinetics have been examined at a dense $La_{0.8}Sr_{0.2}MnO_3$ (LSM) cathode layer deposited on an 8 mol % Y_2O_3-doped zirconia (YSZ) disk, at which only the open perimeter is active, and at a LSM-YSZ composite electrode, where the active sites are distributed throughout the porous matrix. These experiments have been carried out using three-electrode voltammetry (CV) in a variable pO_2 atmosphere (0.03 to 1 atm) at 600 to 900 °C, with the data interpreted using classical Tafel and AH methods. Mass transport effects were ruled out by the lack of dependence of the measured currents on the potential sweep rate and on the gas flow rate.

At the dense LSM film, an α_c of 0.5 and pO_2 dependence of 1 was obtained for the ORR, suggesting that the first electron-transfer step is rate limiting, for example, O_{2ads} to $O_2^-{}_{ads}$. In comparison, at the porous LSM-YSZ composite material, α_c and pO_2 were 0.6 and 0.5, respectively, at low overpotentials, with α_c decreasing to ∼0.25 at high overpotentials. To understand these results, the reaction order with respect to O_2 and the anodic and cathodic transfer coefficients were calculated for four previously proposed ORR mechanisms (mechanisms A to D, Table 5), assuming that the adsorbed reactants and intermediate species obey either Langmuir or Temkin adsorption conditions. Notably, an α_c value of <0.5 cannot be explained using any of the adsorption models or mechanisms examined in this work. Therefore, the rds for the ORR at the porous LSM-YSZ composite cannot be determined using classical Butler−Volmer approaches.

It is concluded that it is more likely that the anomalously low α_c value of <0.5 arises from electrode morphology effects, particularly as it is seen only when the cathode is porous and not when the same LSM-YSZ interface is examined at the dense, single-phase LSM electrode. Indeed, it is known that transfer coefficients can be halved (e.g., from 0.5 to 0.25) when a distributed potential is present in a porous electrode matrix and an analysis of the ORR data using this interpretation is currently underway.[40] In terms of the oxygen evolution reaction (OER), the results suggest that it is limited by either the association of O_{ads} and O_{ads}^{2-} to form $O_2^{2-}{}_{ads}$, or O_{ads} and O_{ads}^- to form $O_2^-{}_{ads}$, assuming that all adsorbed species obey a Temkin adsorption isotherm.

Acknowledgment. This work was supported by The Alberta Energy Research Institute (AERI) through the Coordination of University Research for Synergy and Effectiveness (COURSE) program. The authors also thank Versa Power Systems, particularly Anthony Wood and Tahir Joia, for the provision of materials and useful discussions. We also thank Dr. Yeong Yoo of the National Research Council of Canada (NRC), Ottawa, Ontario, for the donation of the Pt paste and the fabrication of

the dense LSM cathodes, as well as Jeff Soderberg of the University of Calgary for his helpful insights.

References and Notes

(1) Services, E. G.; Parsons, I.; Corporation, S. A. I. *Fuel Cell Handbook*, 5th ed.; U.S. Department of Energy, Office of Fossil Energy, National Energy Technology Laboratory: Morgantown, WV, October 2000.

(2) Mori, D.; Oka, H.; Suzuki, Y.; Sonoyama, N.; Yamada, A.; Kanno, R.; Sumiya, Y.; Imanishi, N.; Takeda, Y. *Solid State Ionics* **2005**, *177*, 535.

(3) Liu, J.; Co, A. C.; Paulson, S.; Birss, V. I. *Solid State Ionics* **2005**, *177*, 377.

(4) Murray, E. P.; Tsai, T.; Barnett, S. A. *Nature* **1999**, *400*, 649.

(5) Wang, S.; Jiang, Y.; Zhang, Y.; Li, W.; Yan, J.; Lu, Z. *Solid State Ionics* **1999**, *120*, 75.

(6) Larrondo, S.; Vidal, M. A.; Irigoyen, B.; Craievich, A. F.; Lamas, D. G.; Fábregas, I. O.; Lascalea, G. E.; Walsöe de Reca, N. E.; Amadeo, N. *Catal. Today* **2005**, *107*−*108*, 53.

(7) Sasaki, K.; Watanabe, K.; Teraoka, Y. *J. Electrochem. Soc.* **2004**, *151*, A965.

(8) Etsell, T. H.; Flengas, S. N. *J. Electrochem. Soc.* **1971**, *118*, 1890.

(9) Adler, S. B. *Chem. Rev.* **2004**, *104*, 4791.

(10) Bockris, J. O. M.; Reddy, A. K. N. *Modern Electrochemistry: an introduction to an interdisciplinary area*; Plenum Publishing Corporation: New York, 1977; Vol. 1.

(11) Bard, A. J.; Faulkner, L. R. *Electrochemical Methods: Fundamentals and Applications*, 2nd ed.; John Wiley & Sons: New York, 2001; Vol. 1.

(12) Erning, J. W.; Hauber, T.; Stimming, U.; Wippermann, K. *J. Power Sources* **1996**, *61*, 205.

(13) Allen, P. A.; Hickling, A. *Trans. Faraday Soc.* **1957**, *53*, 1626.

(14) Østergård, M. J. L.; Clausen, C.; Bagger, C.; Mogensen, M. *Electrochim. Acta* **1995**, *40*, 1971.

(15) Adler, S. B. *J. Electrochem. Soc.* **2002**, *149*, E166.

(16) Adler, S. B.; Henderson, B. T.; Wilson, M. A.; Taylor, D. M.; Richards, R. E. *Solid State Ionics* **2000**, *134*, 35.

(17) Cimenti, M.; Co, A. C.; Hill, J.; Birss, V. I. Manuscript in preparation, 2006.

(18) Co, A. C.; Xia, S. J.; Birss, V. I. *J. Electrochem. Soc.* **2005**, *152*, A570.

(19) Winkler, J.; Hendriksen, P. V.; Bonanos, N.; Mogensen, M. *J. Electrochem. Soc.* **1998**, *145*, 1184.

(20) Boukamp, B. A.; Bouwmeester, H. J. M. *Solid State Ionics* **2003**, *157*, 29.

(21) Macdonald, R. J. *Impedance Spectroscopy: Emphasizing solid materials and systems*; John Wiley & Sons: New York, 1987.

(22) Sirk, A. H. C.; Cambell, S. A.; Birss, V. I. *Electrochem. Solid-State Lett.* **2005**, *8*, A104.

(23) Forster, R. J.; Faulkner, L. R. *J. Am. Chem. Soc.* **1994**, *116*, 5444.

(24) Bockris, J. O. M.; Srinivasan, S. *Fuel Cells: Their Electrochemistry*; McGraw-Hill Book Company: New York, 1969; Vol. 1.

(25) de Levie, R. Electrochemical Response of Porous and Rough Electrodes, 1967.

(26) Perry, M. L.; Newman, J.; Cairns, E. J. *J. Electrochem. Soc.* **1998**, *145*, 5.

(27) Meyer, R. E. *J. Electrochem. Soc.* **1959**, *106*, 930.

(28) Meyer, R. E. *J. Electrochem. Soc.* **1960**, *107*, 847.

(29) Yeager, E.; Huang, J. C.; Clouser, S. J. *J. Appl. Electrochem.* **1993**, *23*, 597.

(30) van Herle, J.; McEvoy, A. J.; Ravindranathan Thampi, K. *Electrochim. Acta* **1996**, *41*, 1447.

(31) Wang, D. Y.; Nowick, A. S. *J. Electrochem. Soc.* **1979**, *126*, 1155.

(32) Takeda, Y.; Kanno, R.; Nada, M.; Tomida, Y.; Yamamoto, O. *J. Electrochem. Soc.* **1987**, *134*, 2656.

(33) Kim, J.-D.; Kim, G.-D.; Moon, J.-W.; Park, Y.-i.; Lee, H.-W.; Kobayashi, K.; Nagai, M.; Kim, C.-E. *Solid State Ionics* **2001**, *143*, 379.

(34) Vetter, K. J.; Manecke, G. *Z. Phys. Chem.* **1950**, *195*, 337.

(35) Hammouche, A.; Siebert, E.; Hammou, A. *Mater. Res. Bull.* **1989**, *24*, 367.

(36) Hammouche, A.; Siebert, E.; Hammou, A.; Kleitz, M.; Caneiro, A. *J. Electrochem. Soc.* **1991**, *138*, 1212.

(37) Carter, S.; Selcuk, A.; Chater, R. J.; Kajda, J.; Kilner, J. A.; Steele, B. C. H. *Solid State Ionics* **1992**, *53*−*6*, 597.

(38) Lee, H. Y.; Cho, W. S.; Oh, S. M.; Wiemhöfer, H.-D.; Göpel, W. *J. Electrochem. Soc.* **1995**, *142*, 2659.

(39) van Heuveln, F. H.; Bouwmeester, H. J. M. *J. Electrochem. Soc.* **1997**, *144*, 134.

(40) Li, Z.; Behruzi, M.; Fuerst, L.; Stover, D. *Proceedings of the Third International Symposium on Solid Oxide Fuel Cell*, May 16−21, 1993, Honolulu, HI; *Proceedings of the Third International Symposium on Solid Oxide Fuel Cell*, May 16−21, 1993, Honolulu, HI, 1993.

(41) Yasuda. *Solid State Ionics* **1996**, *86*−*88*, 1197.

(42) Temkin, M. *Acta Phys. Chim. USSR* **1940**, *12*, 327.

(43) Soderberg, J. N.; Co, A. C.; Sirk, A. H. C.; Birss, V. I. *J. Phys. Chem. B*, in press, 2006.

(44) Gileadi, E.; Conway, B. E. *Modern Aspects of Electrochemistry*; Plenum: New York, 1964; Vol. 3.

(45) Glasstone, S.; Laidler, K. J.; Eyring, H. *The theory of rate processes: the kinetics of chemical reactions, viscosity, diffusion and electrochemical phenomena*; McGraw-Hill: New York, 1941.

(46) Thomas, J. G. N. *Trans. Faraday Soc.* **1961**, *57*, 1603.

(47) Frumkin, A. N. *Z. Physik.* **1926**, *35*, 792.

(48) Flory, P. J. *J. Chem. Phys.* **1942**, *10*, 51.

(49) Conway, B. E.; Angerstein-Kozlowska, H. *J. Electroanal. Chem.* **1980**, *113*, 63.